Crystal structure, magnetism, electronic structure and effect of electron doping in ThCrAsN: An ab-initio study

Smritijit Sen, Najwa Harrati, Adlane Sayede, Houria Kabbour

Crystal structure, magnetism, electronic structure and effect of electron doping in ThCrAsN: An *ab-initio* study

Smritijit Sen[1]*, Najwa Harrati[2], Adlane Sayede[2], Houria Kabbour[1,3]*
[1] *Univ. Lille, CNRS, Centrale Lille, ENSCL, Univ. Artois, UMR 8181 – UCCS – Unité de Catalyse et Chimie du Solide, Lille, 59655 - Villeneuve d'Ascq Cedex, France.*
[2] *Univ. Artois, UMR 8181, Unité de Catalyse et de Chimie du Solide (UCCS), F-62300 Lens, France.*
[3] *Nantes Université, CNRS, Institut des Matériaux de Nantes Jean Rouxel – UMR6502, F-44000, Nantes, France*
* *corresponding author: houria.kabbour@cnrs-imn.fr, smritijit.sen@gmail.com*

In this work, we use first principles methods, to predict a mechanically and dynamically stable crystal structure of ThCrAsN which is iso-structural to ThXAsN (X=Mn,Fe,Co,Ni). We have investigated its mechanical, thermal, magnetic and electronic properties. Our calculation reveals that the magnetic ground state of ThCrAsN is G-AFM. Bader charge analysis reveals a significant interlayer charge transfer between ThN and CrAs layers. Electronic structure of ThCrAsN is thoroughly investigated by evaluation of density of states, band structure and FSs for NM as well as G-AFM phases. Our calculation predicts a metallic behaviour for both the phases. Existence of FS pockets, consisting of multiple Cr-d orbitals at different parts of the Brillouin zone is observed. The influence of electron correlation effects on the electronic structure of ThCrAsN has been investigated using the Hubbard model. We also evaluate Lindhard response function to study the FS nesting which indicate a stronger FS nesting along Γ-X direction as compared to the Γ-M direction. Furthermore, we have examined the alterations in the density of states resulting from the partial substitution of Cr atom with Mn atom in ThCrAsN. Our findings suggest the occurrence of a metal-insulator transition in ThCrAsN upon Mn doping.

I. INTRODUCTION

The compounds of the 1111-type (referred to as ZrCuSiAs-type structure with the space group P4/nmm) have garnered considerable interest due to their ability to manifest a diverse range of magnetic and electrical characteristics through alterations in the combination of transition metals and anions, all while maintaining the same crystal structure [1–7]. The mixed anionic environment enable the extensive tuning of material properties and functionalities leading to various exotic phenomena including high temperature superconductivity [8]. Consequently, these compounds offer a favorable arena for the exploration of physical properties that arise from the interplay of correlated electrons associated with 3d transition metals [9–11]. As an example, the compound LaFeAsO, which serves as the parent compound for the first reported iron-based superconductor by Kamihara *et al.*, possesses a ZrCuSiAs (1111) type structure [12]. This structure consists of alternating layers of $[La_2O_2]^{2+}$ and $[Fe_2As_2]^{2-}$ with an anti-ferromagnetic (AFM) order characterized by spin stripes[13]. Superconductivity in these compounds emerges either through the application of external pressure or via chemical doping. On the other hand, a novel Fe-based superconductor of the 1111-type, ThFeAsN, has recently been unveiled, exhibiting an impressively high superconducting transition temperature (T_c) of up to 30 K in the absence of external pressure or chemical doping[14]. However, several analogous compounds with the same crystal structure but distinct physical properties have been documented. For instance, LaCrAsO exhibits metallic anti-ferromagnetism, whereas LaMnAsO and ThMnAsN demonstrates insulating anti-ferromagnetic behaviour[15–19]. In contrast, LaCoAsO behaves as an itinerant ferromagnet, unlike ThNiAsN and LaNiAsO, which displays Pauli paramagnetism and low-temperature phonon-mediated superconductivity[9, 10, 20]. Although, itinerant ferromagnetism could not be confirmed experimentally upto 1.8 K, emergence of a weak ferromagnetic ordering in ThCoAsN has been predicted theoretically. A notable common characteristic among all these ThXAsN (X=Fe, Co, Ni, Mn) crystal structures is the significantly shorter c-axis as compared to LaXAsO (X=Fe, Co, Ni, Mn) type 1111 compounds. This distinct feature results in an inherent internal chemical pressure, which is believed to exert a significant influence on the diverse array of physical properties exhibited by this series of materials. Cr as well as Cr based alloys are well known for their propensity to exhibit spin density wave (SDW) and Charge density wave (CDW) phenomena [21]. The SDW and CDW phases in Cr and Cr-based alloys is particularly intriguing due to its complex nature and the interplay between magnetic and orbital degrees of freedom. On the other hand, appearance of superconductivity in CrAs under high pressures and $A_2Cr_3As_3$ (A=K, Rb, Cs) under ambient pressure showcases the potential for unconventional superconductivity in Cr-based compounds [22–24]. Co-existence of superconductivity and magnetism is well established in $BaFe_2As_2$ in contrast to the G-type anti-ferromagnetism in $BaCr_2As_2$ [25–28]. Furthermore, a similar compound, $ErCr_2As_2$, with comparable electronic properties, was also identified [29]. Additionally, a series of LnOCrAs (Ln = La, Ce, Pr, and Nd) compounds were synthesized, all exhibiting metallic conduction [15]. LaOCrAs was found to display G-type anti-ferromagnetism with a significant spin moment along the c-axis. These discoveries stimulate further investigations into the underlying mechanisms responsible for SDW/CDW

order, superconductivity and magnetism in these systems, including the role of electron-electron interactions, lattice distortions and electronic band structures. Moreover, dimensionality of the Fermi surface and nesting is intimately connected to the emergence of various intriguing phenomena in condensed matter physics, including spin density waves (SDW), charge density waves (CDW), and even superconductivity [30–36]. The intricate interplay between FS nesting and these phenomena provides valuable insights into the underlying mechanisms that govern the behavior of electrons in materials, paving the way for understanding and potentially harnessing these exotic states of matter.

In this study, we employed *ab-initio* methods to predict a stable crystal structure for ThCrAsN, which is reported very recently [37]. We thoroughly investigated the mechanical, thermal, magnetic, and electronic properties of ThCrAsN. Our calculations indicate that ThCrAsN exhibits a ground state with a magnetic ordering known as G-AFM consistent with the recent experimental and theoretical findings [37]. To understand its electronic structure, we analyzed the density of states, band structure, and Fermi surfaces for both the non-magnetic and G-AFM phases. Additionally, we investigated the impact of electron correlation effects on ThCrAsN's electronic structure using the Hubbard model. We also assessed the degree of Fermi surface nesting in ThCrAsN by evaluating the Lindhard function. Furthermore, we examined the changes in the density of states resulting from the partial substitution of Mn for Cr in ThCrAsN. Our findings suggest that ThCrAsN undergoes a transition from a metallic to an insulating state upon Mn doping. Moreover, our study contribute to the broader understanding of magnetism, electronic structure, electron correlation in this series of materials and pave the way for exploring novel materials.

II. COMPUTATIONAL METHODS

To predict the crystal structure and magnetic ground state of hypothetical ThCrAsN which is synthesized very recently by Wang *et. al.* (2023) [37], we use Universal Structure Predictor: Evolutionary Xtallography (USPEX) [38–40]. USPEX utilizes an evolutionary algorithm coupled with quantum mechanical calculations to explore the vast configuration space of crystals and identify stable or metastable structures. USPEX starts from scratch with a set of randomly generated structures as the initial population, which are then evaluated based on its fitness determined by calculating the total energy of the structure using quantum mechanical calculations. Structures with higher fitness values are selected which then undergo successive genetic operations including mutation and crossover.The population evolves and through the interplay of mutation, crossover, and selection, it gradually converges toward the most stable or lowest energy crystal structures. We perform USPEX calculation interfaced with Vienna ab initio simulation package (VASP) for the fixed composition including magnetic calculation of ThCrAsN using the given parameter settings. We began by randomly generating initial population, consisting of 100 structures. Subsequently, we generated and evaluated 60 generations, each comprising 60 candidates. These 60 generations were created by applying various variation operators to the previously identified structures. These operators included heredity operations (50%), random production (30%), and mutation operators (20%). The numerical USPEX simulation halts once it encounters the identical lowest energy structure in 30 consecutive generations. Using the most stable crystal structure predicted by USPEX code, as a input we carry out first principles calculations with the help of projector augmented-wave (PAW) method as implemented in the numerical code Vienna *ab initio* simulation package (VASP) [41–43]. Exchange correlation functional are treated within the generalized-gradient approximation (GGA) using Perdew-Burke-Ernzerhof (PBE) functional [44]. We also perform GGA+U calculation using the approach of Dudarev *et al.* [45], where the effective Hubbard U is defined as $U_{eff} = U - J$ (U represents the on-site Coulomb repulsion and J represents the exchange interaction). We have done the calculation for U = 1, 3, 5 eV on Cr-d orbital and U = 5, 10, 12 eV on Th-f orbital. We construct a $\sqrt{2} \times \sqrt{2} \times 2$ magnetic super-cell to implement various antiferromagnetic (AFM) spin arrangements. We expand the wave functions in the plane wave basis with an energy cutoff of 550 eV and the energy tolerance value for the self-consistent calculations are set at 10^{-6} eV. The sampling of the Brillouin zone (BZ) is performed using a Γ-centered $6 \times 6 \times 3$ Monkhorst-Pack grid. Elastic constants were evaluated within VASP by finite differences of stress with respect to strain [46]. For the Fermi surface and density of states calculations, a denser k-grid is employed. Visualisation of Fermi surfaces are done by the Fermi surfer software [47]. The Crystal orbital Hamilton population (COHP) analysis are performed in the framework of the LOBSTER software [49–51]. Phonon calculation has been carried out within density functional perturbation theory using the VASP code interfaced with PHONOPY software [52] codes. To model the disordered system with Mn doping on Cr site, we use a large supercell containing 32 Cr atoms.

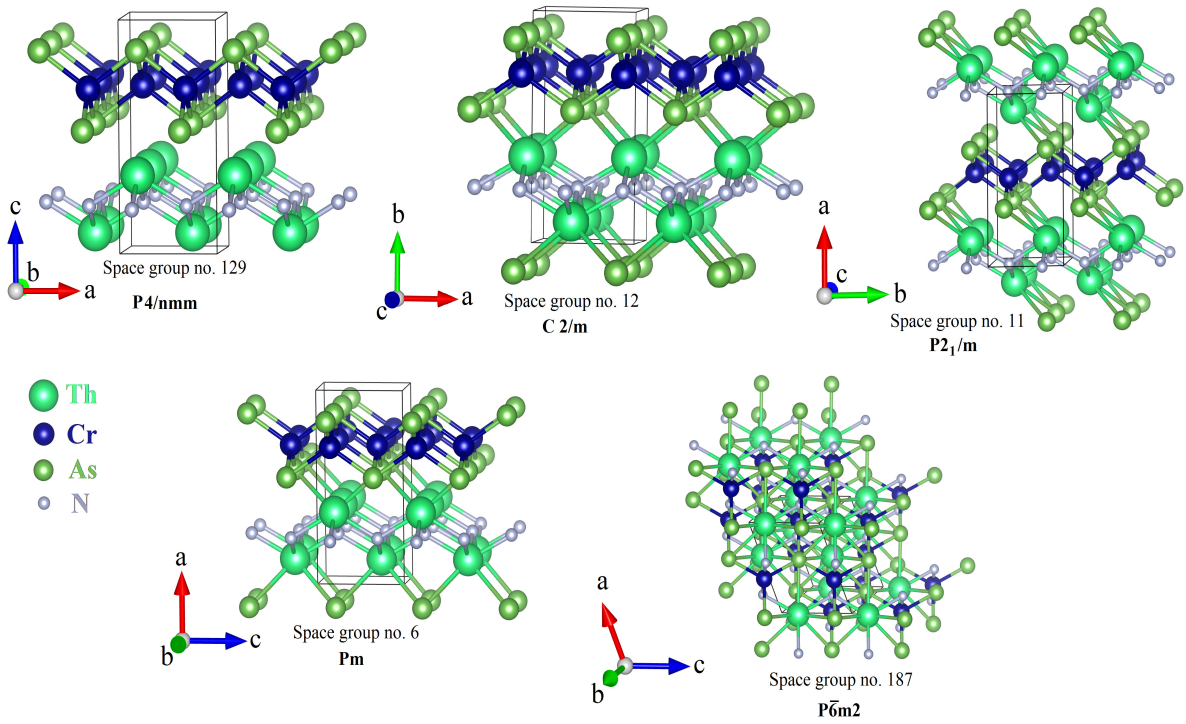

FIG. 1: Structures predicted using the USPEX code.

III. RESULTS AND DISCUSSION

A. Crystal structure prediction

Five most stable crystal structures predicted by our USPEX calculation are depicted in FIG.1. Among them tetragonal crystal structure with P4/nmm symmetry (space group no 129) has the lowest enthalpy (best fitness value). We also enable magnetic calculation in USPEX interfaced with VASP to search for the spin states. The predicted ground state exhibits a high spin configuration with magnetic moment 2.65 μ_B. All the compounds synthesized in this ThXAsN (X=Mn, Fe, Co, Ni) series possess the P4/nmm symmetry and as far as our calculation is concern ThCrAsN is not an exception of it. A very recent synthesis of ThCrAsN crystal confirms our claim . However, other crystal structure predicted by USPEX with a higher enthalpy than the tetragonal crystal structure with P4/nmm symmetry might be obtainable under high temperature and/or high pressure conditions. Cell volumes and enthalpies of all the USPEX predicted "good structures" are presented in the supplementary material. All the crystallographic models, except the model with space group 187 (P$\bar{6}$m2), exhibit a layered structure characterized by typical ThN and CrAs layers and share similar structures with slight variations in symmetry. It's noteworthy that the first four models, as proposed by USPEX, are related to the ZrSiCuAs structural type, highlighting the accuracy of USPEX in predicting this composition's stability. This underscores the robustness of the ZrSiCuAs structure for this composition. In contrast, the fifth potentially stable model, with space group 187 (P$\bar{6}$m2), do not exhibit a low (2D) structuration. What's particularly intriguing in this case is the presence of a mixed anion environment for all cations (and a mixed cationic environment for all anions). For instance, chromium (Cr) forms mixed anion trigonal bipyramids with both nitrogen (N) and arsenic (As), creating CrN_2As_3 polyhedra. Additionally, thorium (Th) is surrounded by three N atoms and four As atoms, forming ThN_3As_4 polyhedra. In contrast, in the layered structure, there is notable ionic segregation as Cr is exclusively surrounded by As anions, while N is surrounded only by Th cations, which is nothing but a consequence of the layered character of the structure. The highly mixed environments observed in the last model hold significant scientific interest and might be attainable through non-standard synthesis techniques, such as high-pressure methods. Our calculation also predicted a high spin state of Cr atom in ThCrAsN which can be confirmed by experiments. The outermost electronic configuration of Cr^{2+} is $3d^4$. In the high spin complexes of Cr^{2+} number of unpaired electron is 4. Therefore, the predicted value of Cr local magnetic moment 2.65 μ_B can be justified from the filling of d orbitals consistent with Hund's rule (gS=4μ_B). Now, in the next section, we will use

this USPEX predicted tetragonal crystal structure (lattice parameters and atomic positions) to determine the precise magnetic ground state of ThCrAsN.

B. Magnetism

TABLE I: Ground state energies (with respect to NM state), structural parameters (lattice constants and atomic positions) and local magnetic moment of Cr for ThCrAsN with various spin configurations.

Spin configuration	Energy (meV/f.u.)	a (Å)	c (Å)	V (Å^3)	z_{Th}	z_{As}	Cr moment (μ_B)
NM	0	3.938	9.167	142.16	0.1327	0.6633	0
FM	-299.6	4.117	8.647	146.54	0.1312	0.6540	2.29
A-AFM	-300.4	4.115	8.679	146.96	0.1311	0.6529	2.30
C-AFM	-362.9	4.055	8.947	147.12	0.1304	0.6645	2.65
G-AFM	-363.6	4.052	8.943	146.83	0.1306	0.6650	2.65
S-AFM	-169.5	4.046*	8.966	148.08	0.1294	0.6625	2.56

* orthorhombic, a$\neq b$, b=4.081Å.

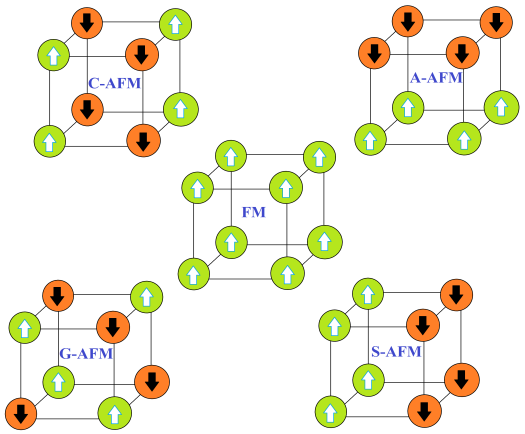

FIG. 2: Schematic representation of Ferromagnetic (FM), C-type antiferromagnetic (AFM), A-type antiferromagnetic (C-AFM), G-type antiferromagnetic (G-AFM) and Spin-stripe antiferromagnetic spin arrangements for Cr atoms in $\sqrt{2} \times \sqrt{2} \times 2$ supercell of tetragonal P4/nmm ThCrAsN.

To determine the magnetic ground state of ThCrAsN, we perform spin polarised calculation for various magnetic spin configuration of Cr atom and then compare the ground state energies of each spin configuration along with the non-magnetic ground state energy (estimated using non spin polarised calculation). The spin configuration with the lowest total energy is considered to be the magnetic ground state. We consider four different anti-ferromagnetic (AFM) spin arrangements along with the ferromagnetic (FM) spin configuration as depicted in FIG.2. Four AFM spin configurations of Cr in ThCrAsN are A type anti-ferromagnet (A-AFM), C type anti-ferromagnet (C-AFM), G type anti-ferromagnet (G-AFM) and spin stripe type anti-ferromagnet (S-AFM). In TABLE-I, we present our calculated values of ground state energies, lattice parameters, atomic positions, volume of unit cell and Cr local magnetic moment for all the spin configurations. Ground state energies of all the spin configurations are evaluated with respect to the ground state energy of non magnetic (NM) ThCrAsN. Our calculation reveals that the ground state energy of G-AFM spin configuration has the lowest among all together spin configurations that we considered. C-type anti-ferromagnet involves anti-parallel alignment within the planes and ferromagnetic alignment between the planes, while G-type anti-ferromagnet involves anti-parallel alignment in both the directions. Energy difference of ThCrAsN with C-AFM and G-AFM spin configuration is not very significant (0.7 meV) which indicate a weak magnetic coupling between

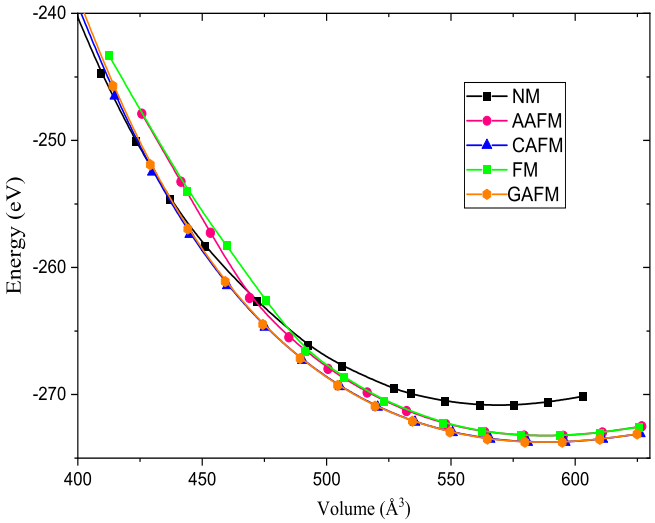

FIG. 3: Energy vs. volume curve for Non-magnetic (NM), Ferromagnetic (FM), C-type antiferromagnetic (AFM), A-type antiferromagnetic (C-AFM), G-type antiferromagnetic (G-AFM) spin arrangements for Cr atoms in tetragonal P4/nmm ThCrAsN.

out of plane Cr atoms. Electronic structure of ThCrAsN with C-AFM, A-AFM, S-AFM and FM spin configurations are presented in the supplementary material. Spin polarised geometry optimization of ThCrAsN with different spin arrangements yields a optimized tetragonal structure for all the cases with no alteration of initial symmetry of P4/nmm except for S-AFM. For the S-AFM, we obtain orthorhombic crystal structure (a$\neq$ b) after performing the spin polarised geometry optimization. Our calculated value of Cr local magnetic moment (2.65 μ_B) for G-AFM matches with the USPEX prediction. This value of Cr magnetic moment 2.65 μ_B can be comparable with the theoretically computed Cr local magnetic moment 2.60 μ_B of LaCrAsO. However, experimentally measured value of Cr magnetic moment in LaCrAsO is 1.57 μ_B at room temperature (Cr magnetic moment was not measured below room temperature). This discrepancy is due to the thermal fluctuation in room temperature [15]. In FIG.3, we display energy versus volume curve for all the tetragonal crystal structure of ThCrAsN with various spin configurations. Our results reveal that at lower volume, non magnetic state can be achieved and applying hydrostatic pressure can be a way to compress a crystal structure. We have also perform COHP calculation for the Cr-Cr bond in ThCrAsN for G-AFM as well as

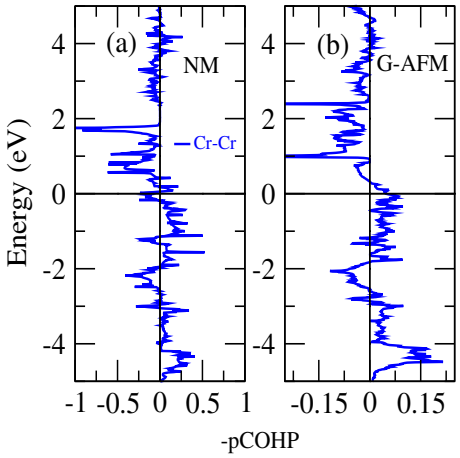

FIG. 4: COHP bonding analysis of Cr-Cr bonds in ThCrAsN for (a) NM and (b) GAFM phase

NM structure. In FIG.4, we depict the projected COHP for the NM and G-AFM spin configuration in ThCrAsN. Positive values of -pCOHP delineate bonding energy regions whereas negative values bear the signature of antibonding states. For NM ThCrAsN, we can clearly see that a significant amount of antibonding states at the Fermi level which makes the system unstable. On the other hand, ThCrAsN for G-AFM spin arrangement, no antibonding states exists

near the Fermi level. Therefore, G-AFM state is more favourable than the NM one at ambient condition. Metallic G-AFM spin state has also been established experimentally as well as theoretically in LaCrAsO. However, ThMnAsN possesses C-AFM spin arrangement with a small energy gap at the Fermi level as revealed by the recent experimental and theoretical results. In the forthcoming sections, we will discuss the mechanical and dynamical stability as well as electronic structure of ThCrAsN with G-AFM spin configuration.

C. Mechanical and dynamical stability

TABLE II: Calculated elastic constants (C_{ij}), bulk modulus (B), shear modulus (G), and Young's modulus (Y) in GPa as well as Poisson's ratio (ν) and Debye temperature (Θ_D) of ThCrAsN.

C_{11}	C_{12}	C_{13}	C_{33}	C_{44}	C_{66}	B	G	Y	ν	Θ_D (K)
182	30	64	98	42	52	85	44	113	0.28	288

In this section, we will discuss the mechanical and dynamical stability of ThCrAsN. Our estimated elastic constants and elastic moduli are presented in TABLE-II. The total number of independent elastic constants depends on the symmetry of the crystal structure. For instance, a cubic crystal has only three independent elastic constants. For tetragonal ThCrAsN crystal structure, we have obtained six independent elastic constants. All calculated elastic constants are positive and obey the well-known Born criterion of mechanical stability. It is quite evident from our calculations that the value of elastic constant C_{33} is well above the limit of the elastic stability, *i.e.*, $C_{33} > 2C_{13}^2/(C_{11}+C_{12})$. By applying the Voigt-Reuss-Hill (VRH) approximation [53], the macroscopic bulk modulus (B), shear modulus (G) and Young's modulus of polycrystalline ThCrAsN can be evaluated from the elastic constants of the single crystal, depicted in TABLE-II. A material is considered to be ductile if it satisfies the well-known Pough's criterion $B/G > 1.75$. For ThCrAsN, the value of B/G=1.91 which suggest ductile behaviour. In FIG.5, phonon dispersion and phonon density

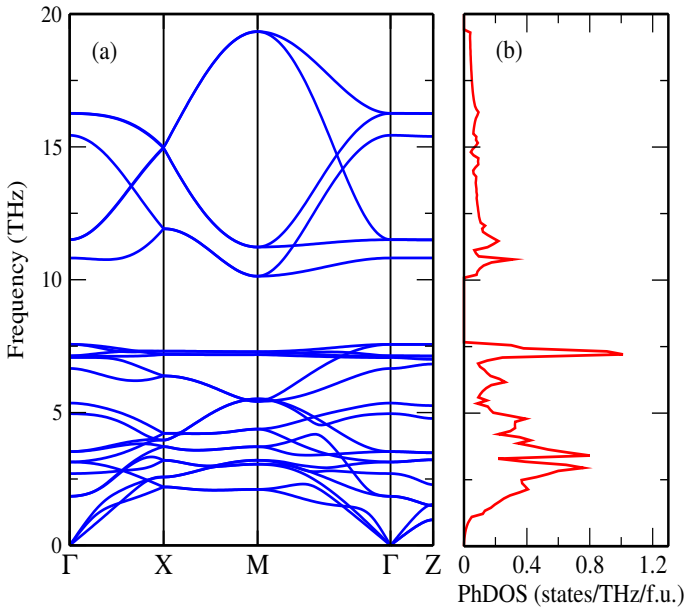

FIG. 5: (a) Phonon dispersion and (b) phonon density of states of ThCrAsN with G-AFM spin configuration.

of states are presented. In a dynamically stable material, all phonon frequencies are real (non-imaginary) throughout the entire Brillouin zone. This implies that the lattice vibrations are physically meaningful and can propagate without exponentially growing or decaying amplitudes. The absence of imaginary frequencies in ThCrAsN ensures that the vibrational modes do not lead to an instability in the crystal structure. We have also observe that a clear phononic band gap exists between the optical and acoustic phonons. The behavior of phonons, such as their dispersion relations, vibrational modes, and scattering mechanisms, influences thermal conductivity, heat capacity and thermal transport

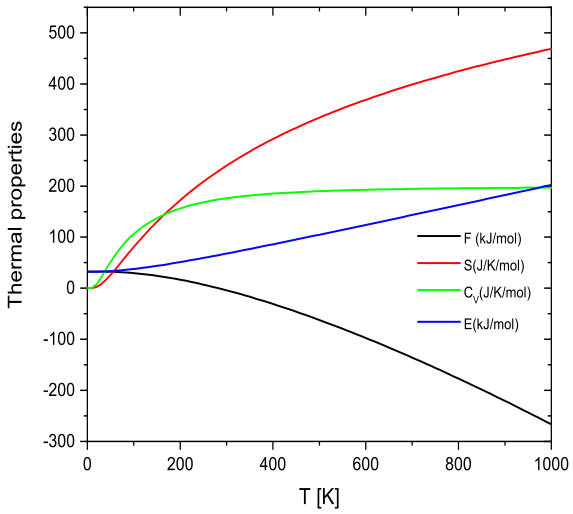

FIG. 6: Thermodynamic properties of ThCrAsN

properties of solids. In FIG.6, we depict free energy, entropy, specific heat at constant volume and internal energy of ThCrAsN as a function of temperature. These predicted thermodynamic properties are useful to report for future studies as thermodynamics plays a significant role in understanding and predicting crystal growth processes.

D. Bader charge analysis

We perform Bader charge analysis of ThCrAsN for G-AFM spin configuration and the outcomes are presented in TABLE.III. Net bader charges elucidate the manner in which electron density is distributed among individual atoms within a system, thereby offering valuable insights into the electronic structure. Positive bader charges signify an acquisition of electron density by an atom, whereas negative charges indicate a loss of electron density when compared to the reference state. Since ThCrAsN consists of alternating layers of ThN and CrAs, the charge transfer between the layers are also studied. An electron deficiency of 0.60 is observed in the CrAs layer of ThCrAsN. This value is quite high as compared to the other systems in this ThXAsN (X=Mn, Fe, Co, Ni) series of materials. In ThFeAsN, ThCoAsN and ThNiAsN, a loss of 0.38, 0.51 and 0.40 electrons in the $[Fe/Co/NiAs]^-$ layer was found, respectively [4]. High charge transfer between neighboring layers signifies a strengthening of the ionic nature in the inter-layer bonding. Consequently, the inter-layer bonds in ThCrAsN, which play a crucial role in maintaining the crystal's overall stability, is stronger.

TABLE III: Bader charge analysis of ThCrAsN.

Species	Valency	Bader charge	net Bader charge
Th	12	9.78	2.22
Cr	12	11.37	0.63
As	5	6.23	-1.23
N	5	6.62	-1.62
(ThN)	17	16.40	0.60
(CrAs)	17	17.60	-0.60

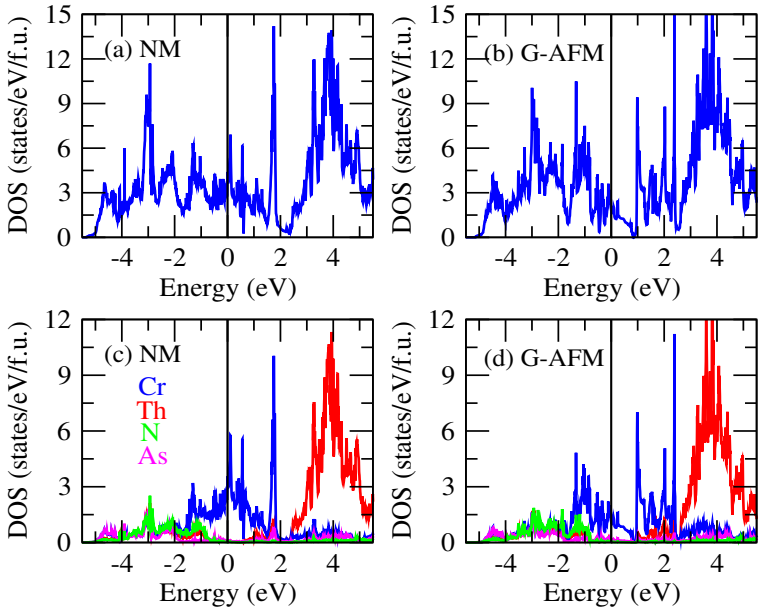

FIG. 7: Calculated (a, b) total and (c, d) atom projected density of states of ThCrAsN for non-magnetic and G-AFM spin configuration. Fermi level is denoted by a vertical black line at E = 0 eV.

E. Electronic structure

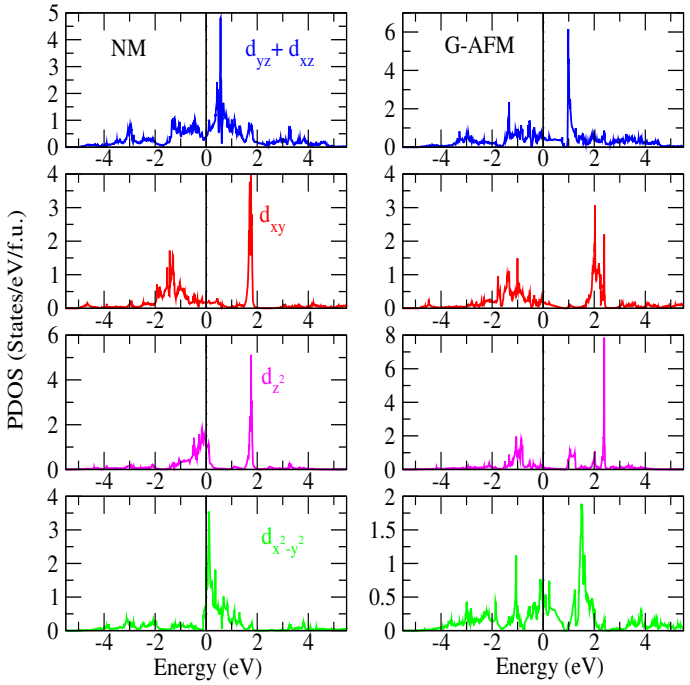

FIG. 8: Cr-d orbital projected density of states of ThCrAsN for non-magnetic (left column) and G-AFM spin configuration (right column).

We studied the electronic structure of ThCrAsN in terms of density of states, band structure and Fermi surfaces. Since G-AFM stands out as the lowest energy state at ambient condition, we focus on the electronic structure of G-AFM phase of ThCrAsN manifested by density of states, band structure and FSs. Since for the implementation

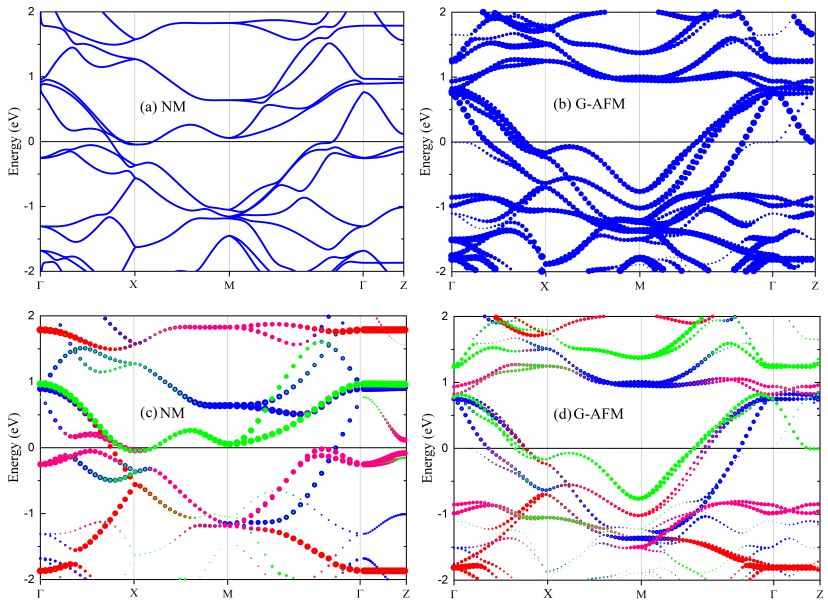

FIG. 9: Calculated band structure of ThCrAsN for (a) non-magnetic and (b) G-AFM spin configuration. Cr-d orbitals projected band structure for (c) non-magnetic and (d) G-AFM spin configuration. Cr d_{xz+yz}, d_{xy}, d_{z^2} and $d_{x^2-y^2}$ orbitals are denoted by blue, red, magenta and green colours respectively.

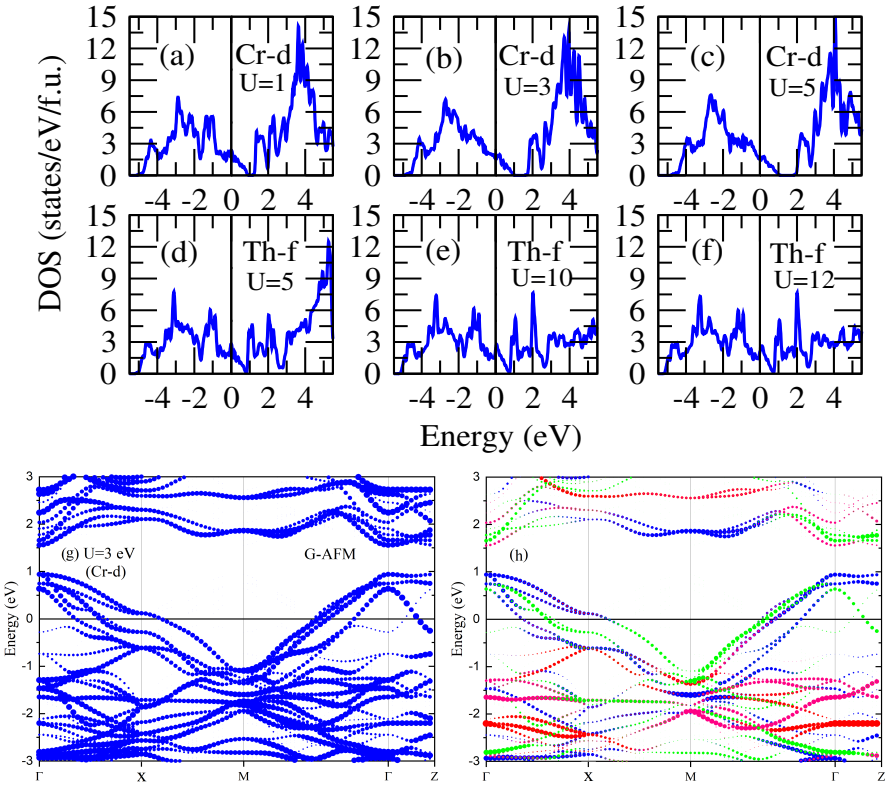

FIG. 10: (a-f) Calculated total density of states of ThCrAsN for G-AFM spin configuration with Hubbard U. (g) Calculated band structure of ThCrAsN for G-AFM spin configuration with Hubbard U=3 eV in Cr-d orbitals. (h) Cr-d orbitals projected band structure for the same.

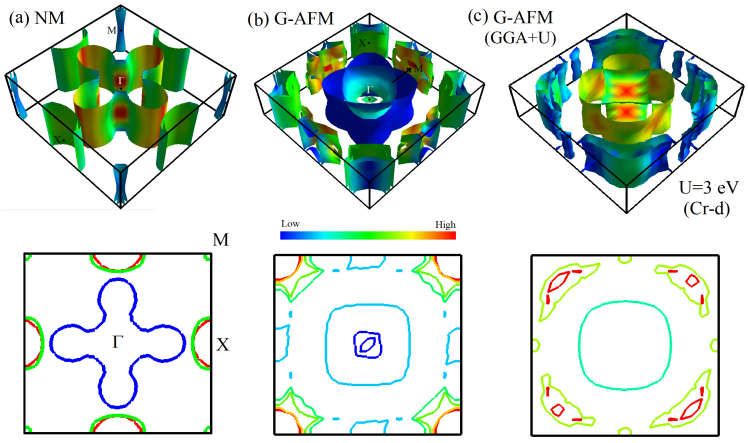

FIG. 11: Calculated Fermi surfaces of ThCrAsN for (a) non-magnetic and (b) G-AFM spin configuration ($\sqrt{2} \times \sqrt{2} \times 2$ supercell) and (d) with Hubbard U=3 eV in Cr-d orbitals (G-AFM) shaded by band velocity (top panel). Fermi surface sections in 001 plane at k_z=0 for the same in the lower panel

of G-AFM spin arrangement in ThCrAsN, we construct a $\sqrt{2} \times \sqrt{2} \times 2$ supercell, electronic band structures will get folded into the smaller Brillouin zone (BZ). We use band unfolding technique to extend the electronic band structure of ThCrAsN with G-AFM spin configuration calculated within a reduced BZ to the full or larger BZ. Non-magnetic electronic structure of ThCrAsN is also presented for a comparison. We have also studied the electronic structure of ThCrAsN with G-AFM spin configuration calculated using GGA+U method. The Hubbard U correction is introduced to account for the on-site Coulomb repulsion between localized electrons. It is based on the Hubbard model, which describes a simplified system of localized electrons on atomic orbitals. The parameter U represents the energy cost of adding two electrons to the same localized orbital. In FIG.7(a, b), total density of states are displayed for NM and G-AFM ThCrAsN. It is quite evident from FIG.7 that both NM as well as G-AFM states are metallic in nature. Atom projected density of states, displayed in FIG.7(c, d) suggest the domination of Cr-d orbitals at the Fermi level for NM and G-AFM phases. However for G-AFM spin configuration, we observe a moderate contribution of As-p orbital at the Fermi level in ThCrAsN. The Th-5d and 4f orbitals predominantly occupy energy levels above 3 eV and are primarily unoccupied. On the other hand, the N 2p states reside below the Fermi level within the energy range of -1 to -4 eV, suggesting that the ThN layers do not actively participate in electronic conduction but instead act as a "blocking layer" as observed in other ZrSiCuAs type structure [54]. A very high density of states contribution from Cr atom at the Fermi level of NM ThCrAsN may leads to stoner instability. The high density of states at the Fermi level can also imply a enhanced electron-electron interactions. These interactions can result in various phenomena, such as strong correlations, magnetism, superconductivity, or other collective electronic behaviors. The presence of many available states can facilitate electron scattering and promote the formation of ordered states or electronic instabilities [55]. We further study the Cr-d orbital projected density of states, presented in FIG.8. There is a noticeable difference in Cr-d orbital contributions at the Fermi level between NM and G-AFM ThCrAsN. Although all five Cr-d orbital constitute the Fermi level of NM and G-AFM ThCrAsN, d_{xz+yz} orbitals pre-eminence the Fermi level for G-AFM in contrast to the dominance of d_{z^2} and $d_{x^2-y^2}$ orbitals at the Fermi level for the case of NM ThCrAsN. In FIG.9 (a, b), our calculated band structures of NM and G-AFM ThCrAsN are displayed. Same multi-orbital character also reflected in our calculated Cr-d orbital projected band structure depicted in FIG.9 (c, d). This constitute a Multi-orbital FSs which provide additional degrees of freedom to tune the electronic properties of a material. By selectively modifying the occupation or coupling of specific orbitals, it is possible to manipulate the band structure, transport properties, and magnetic behavior of the material. This tunability can be leveraged for various applications, including electronic devices and materials design. In FIG.10, we exhibit our calculated density of states as well as band structure with the inclusion of Hubbard U correction in ThCrAsN with G-AFM spin arrangement. Hubbard U correction is considered for Cr-d as well as Th-f orbitals. For all the cases, we notice metallic behaviour. We also observe that with the introduction of U (5 eV, 10 eV, 12 eV) in Th-f orbital, there is no significant modification in the density of states near Fermi level (-4 eV to 4 eV) as evident from FIG.10 (d-f) and FIG.7b. On the other hand, if we compare FIG.7b and FIG.9b with our calculated density of states and band structure, invoking the Hubbard U in Cr-d orbital manifested in FIG.10 (a-c) and FIG.10g, appearance of a energy gap around 1 eV (above Fermi level) can be seen. This energy gap increases with the increasing strength of U in Cr-d orbital (The estimated value of the energy gap is approximately 0.5 eV and 1 eV for U=3 eV and U= 5eV respectively). However, orbital character near Fermi level is not altered

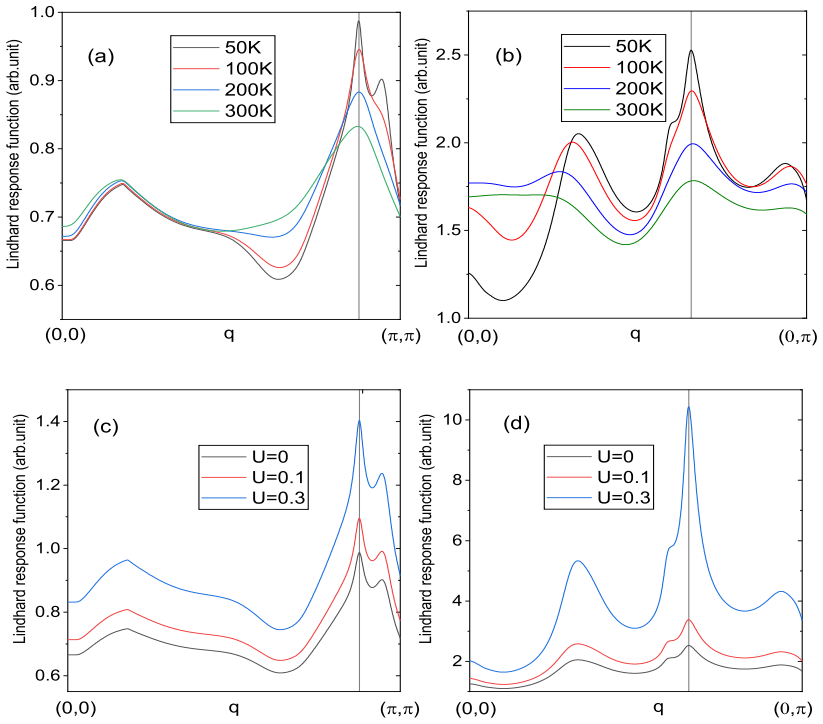

FIG. 12: (a, b) Lindhard response function of ThCrAsN along the Γ-M and Γ-X direction for different temperature and (c, d) its variation with Coulomb interaction strength U at 50K.

as apparent from FIG.10h. Energy gap above the Fermi level affects properties such as optical absorption, emission and higher energy excitations. This also give a indication that a metal-insulator transition can occur in ThCrAsN upon electron doping. In FIG.11, we present our simulated FSs of ThCrAsN for NM and G-AFM spin configuration. Effect of Hubbard U (3 eV in Cr-d) on the FSs are shown in FIG.11c. Lower panel in FIG.11 demonstrates the FS sections in 001 plane at K_z=0 which can be compared with the experimentally measured ARPES data if available. However, our computed FSs of ThCrAsN is quite similar to the simulated FSs of LaCrAsO. Presence of FS sheets at the different part of the BZ in ThCrAsN opens up a possibility of FS nesting. The nesting condition allows for the efficient scattering of electrons between the nested regions, leading to the formation of CDW or SDW. In the next section, we will study this FS nesting effect by evaluating the Lindhard function which describes the response of a Fermi liquid to an external perturbation, particularly in the context of electronic excitations.

F. Nesting Properties of non-magnetic ThCrAsN

The nesting effect is determined by calculating the static Lindhard function for non-magnetic ThCrAsN, which is given by,

$$\chi(q) = -\frac{1}{N}\sum_{k}\frac{f(E_k) - f(E_{k+q})}{E_k - E_{k+q}}$$

where N is the number of k points in the sum, f is the Fermi-Dirac distribution function, E_k and E_{k+q} are the band eigenvalues obtained by DFT calculations. In FIG.12 (a, b), we present our calculated Lindhard response function along the Γ-M and Γ-X directions for different temperatures. Γ (0,0), M (π,π) and X (0,π) points are the high symmetry points in the BZ as pointed out in FIG.11a. In a nested Fermi surface, certain portions of the FS can be maped to another part of the FS by a vector in momentum space, called nesting vector. In some cases, the presence of nesting can enhance the response of a material to the external perturbations and lead to the formation of sharp peaks in the Lindhard function. This is particularly relevant in the study of superconductors and other systems exhibiting charge-density wave or spin-density wave instabilities. We can clearly see two peaks in the Lindhard function calculated along Γ-M direction in contrast to the three peaks along Γ-X direction. These peaks indicate different intra and inter band nesting processes between the three sets of FSs. Along Γ-M direction a sharp peak is observed at 0.88q. On the other hand, at 0.66q largest peak appear in the Lindhard function along Γ-X direction. Overall degree of nesting is more significant along Γ-X direction than along Γ-M directions. Lowering of temperature enhances the magnitude of Lindhard response function. However, all the nesting vectors corresponding to the nesting processes along Γ-X and Γ-M directions are independent of temperature with the one exception as the first peak in the Lindhard response function along Γ-X direction shifts with the variation of temperature. Now, we include electron-electron interactions within random phase approximation (RPA) which incorporates the effects of electron-electron interactions through the introduction of an effective interaction. This effective interaction accounts for the screening of the Coulomb interaction by the surrounding electrons. By considering these interactions, the RPA captures the collective behavior of the electrons, leading to an enhanced response given by,

$$\chi_q^{\mathrm{RPA}} = \frac{\chi_{\mathrm{q}}}{1 - U\chi_{\mathrm{q}}}$$

where U is the interaction strength parameter. In FIG.12(c, d), we depict the RPA enhanced Lindhard response function along Γ-X and Γ-M directions for interaction strength U=0.1 and 0.3. Clearly, a significant enhancement of the Lindhard response peaks along Γ-X direction is observed.

G. Effect of electron doping and metal-insulator transition

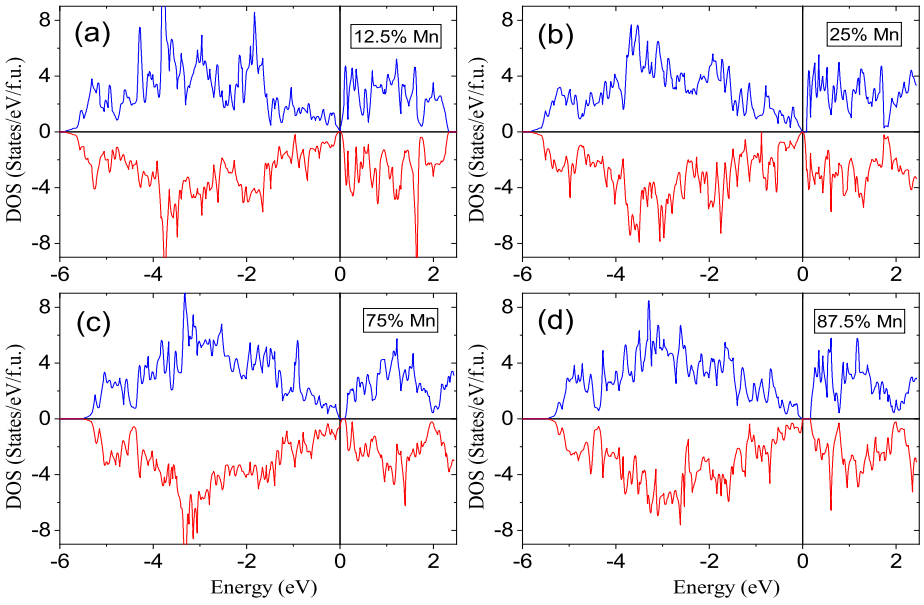

FIG. 13: Calculated density of states of $ThCr_{1-x}Mn_xAsN$ with G-AFM spin configuration with (a) 12.5% (b) 25% (c) 75% (d) 87.5% Mn doping.

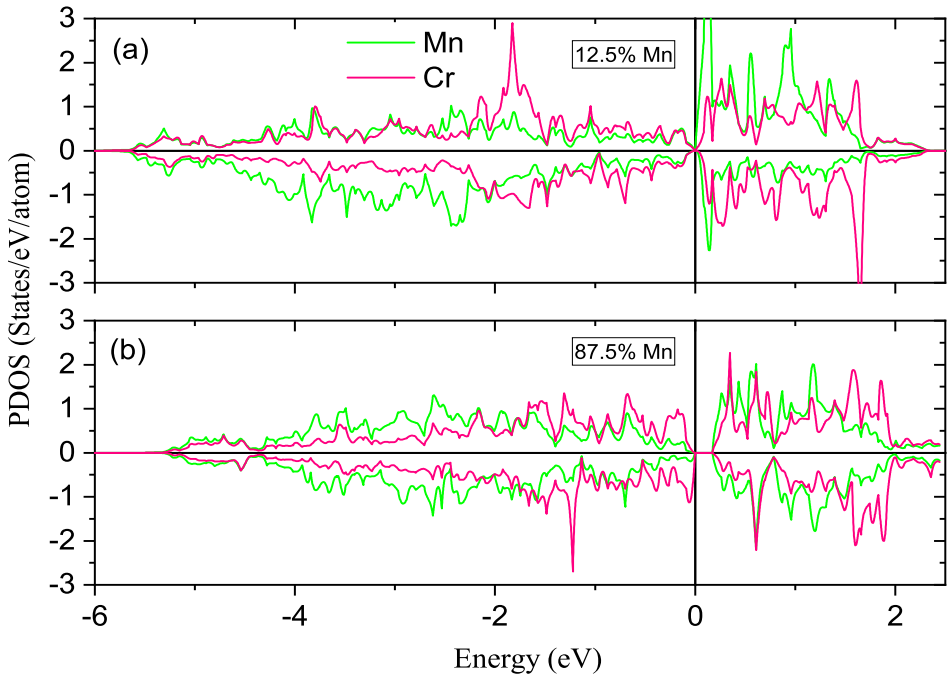

FIG. 14: Calculated Cr and Mn atom projected density of states of $ThCr_{1-x}Mn_xAsN$ with G-AFM spin configuration with (a) 12.5% and (b) 87.5% Mn doping.

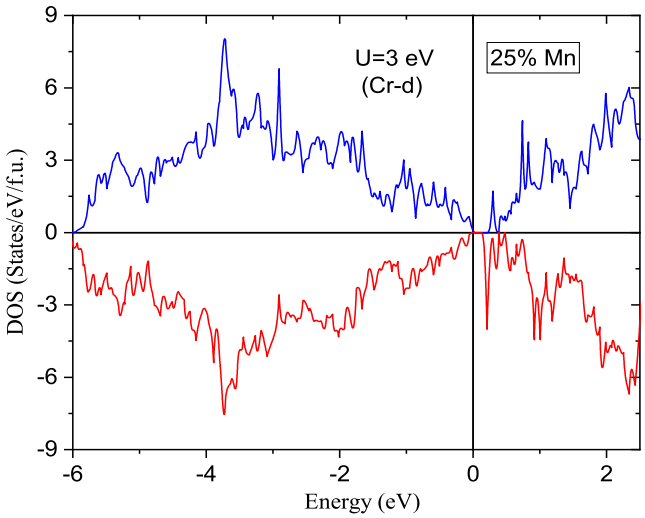

FIG. 15: Calculated density of states of $ThCr_{1-x}Mn_xAsN$ with Hubbard U=3 eV in Cr-d orbital for 25% Mn doping.

In this section, we will discuss the effect of electron doping on the electronic structure of ThCrAsN. Oxygen substitution in Nitrogen sites (electron doping) in ThCrAsN has recently been synthesized with no superconductivity [37]. In this work, we studied the Mn substitution in Cr sites which is equivalent to electron doping. In that purpose, a very large super-cell is considered for the distribution of Cr and Mn in the transition metal sites. We have also considered the G-AFM spin configuration in these disordered structure with various Mn doping concentrations. Density of states of $ThCr_{1-x}Mn_xAsN$ for various Mn doping concentrations are presented in FIG.13. At around 25%

Mn doping, a metal insulator transition occurs which is also observed in $LaCr_{1-x}Mn_xAsO$ with x 0.2. If we increase the amount of Mn doping, the energy gap at the fermi level also increased. It is noteworthy to mention here that a small energy gap is seen in ThMnAsN with C-AFM ground state. Projected density of states of Cr and Mn atoms are depicted in FIG.14 for 12.5% and 87.5% Mn doping. We have also employed Hubbard U (3 ev) on Cr and Mn 3d orbitals for evaluation of density of states in $ThCr_{1-x}Mn_xAsN$ with x=0.25 and presented in FIG.15. We find that the energy gap at the Fermi level for the Mn substituted ThCrAsN increases when we include electron correlation within Hubbard model.

H. Summary and conclusions

In summary, by using *ab-initio* methods, we have predicted a mechanically and dynamically stable crystal structure of ThCrAsN which is iso-structural to ThXAsN (X=Mn,Fe,Co,Ni). We have investigated its mechanical, thermal, magnetic and electronic properties. Our calculation reveals that the magnetic ground state of ThCrAsN is G-AFM which is consistent with our COHP results. Our Bader charge analysis, indicate a significant amount of inter-layer charge transfer in ThCrAsN. Electronic structure of ThCrAsN is thoroughly investigated by the evaluation of density of states, band structure and FSs for NM as well as G-AFM phases. Both the NM as well as G-AFM states of ThCrAsN show metallic behaviour with the Fermi surfaces constitute of multiple Cr-d orbitals. We also evaluate Lindhard function to study the FS nesting. It appears that the degree of FS nesting along Γ-X direction in the BZ is much stronger than FS nesting along Γ-M direction. Our results also stipulate a metal-insulator transition in ThCrAsN with Mn substitution in Cr sites. The inclusion of electron correlation within the Hubbard model leads to an elevation in the energy gap at the Fermi level for Mn-substituted ThCrAsN.

I. Acknowledgements

This work was supported by the I-Site (ANR-16-IDEX-0004 ULNE) and by the ANR (project ANR-21-CE08-0051). The regional computational cluster (Mesocentre-Lille) is thanked for providing computational resources.

[1] I. Troyan, A. Gavriliuk, R. Rüffer, A. Chumakov, A. Mironovich, I. Lyubutin, D. Perekalin, A. P. Drozdov, M. I. Eremets, Observation of superconductivity in hydrogen sulfide from nuclear resonant scattering. *Science* **2016**, 351, 1303.
[2] R. Pöttgen, D. Johrendt, Materials with ZrCuSiAs-type Structure. *Z. Naturforsch. B: J. Chem. Sci.* **2008**, 63, 1135.
[3] P. Quebe, L. J. Terbüchte, W. Jeitschko, Quaternary rare earth transition metal arsenide oxides RTAsO (T=Fe, Ru, Co) with ZrCuSiAs type structure. *J. Alloys Compd.* **2000**, 302, 70.
[4] S. Sen, G. -Y. Guo, Electronic structure, lattice dynamics, and magnetic properties of ThXAsN (X= Fe, Co, Ni) superconductors: A first-principles study. *Phys. Rev. B* **2020**, 102, 224505.
[5] K. Ishida, Y. Nakai, H. Hosono, To What Extent Iron-Pnictide New Superconductors Have Been Clarified: A Progress Report. *J. Phys. Soc. Jpn.* **2009**, 78, 062001.
[6] T. C. Ozawa, S. M. Kauzlarich, Chemistry of layered d-metal pnictide oxides and their potential as candidates for new superconductors. *Sci. Technol. Adv. Mater.* **2008**, 9, 033003.
[7] S. Sen, G. -Y. Guo, Pressure induced Lifshitz transition in ThFeAsN. *Phys. Rev. Materials* **2020**, 4, 104802.
[8] H. Kageyama, K. Hayashi, K. Maeda, J. P. Attfield, Z. Hiroi, J. M. Rondinelli, K. R. Poeppelmeier, Expanding frontiers in materials chemistry and physics with multiple anions. *Nature Communications* **2018**, 9, 772.
[9] T. Watanabe, H. Yanagi, Y. Kamihara, T. Kamiya, M. Hirano, H. Hosono, Nickel-based layered superconductor, LaNiOAs. *J. Solid State Chem.* **2008**, 181, 2117.
[10] H. Yanagi, R. Kawamura, T. Kamiya, Y. Kamihara, M. Hirano, T. Nakamura, H. Osawa, H. Hosono, Itinerant ferromagnetism in the layered crystals LaCoOX (X = P, As). *Phys. Rev. B* **2008**, 77, 224431.
[11] A. Marcinkova, T. C. Hansen, C. Curfs, S. Margadonna, J. -W. G. Bos, Nd-induced Mn spin-reorientation transition in NdMnAsO. *Phys. Rev. B* **2010**, 82, 174438.
[12] Y. Kamihara, T. Watanabe, M. Hirano, H. Hosono, Iron-Based Layered Superconductor $La[O_{1-x}F_x]FeAs$ (x = 0.05-0.12) with T_c = 26 K. *J. Am. Chem. Soc.* **2008**, 130, 3296.
[13] S. Muir, M. A. Subramanian, ZrCuSiAs type layered oxypnictides: A bird's eye view of LnMPnO compositions. *Prog. Solid State Chem.* **2012**, 40, 41.
[14] C. Wang, Z. C. Wang, Y. X. Mei, Y. K. Li, L. Li, Z. T. Tang, Y. Liu, P. Zhang, H. F. Zhai, Z. A. Xu, G. H. Cao, A New ZrCuSiAs-Type Superconductor: ThFeAsN. *J. Am. Chem. Soc.* **2016**, 138, 2170.
[15] S. W. Park, H. Mizoguchi, K. Kodama, S. Shamoto, T. Otomo, S. Matsuishi, T. Kamiya, H. Hosono, Magnetic structure and electromagnetic properties of LnCrAsO with a ZrCuSiAs-type structure (Ln = La, Ce, Pr, and Nd). *Inorg. Chem.* **2013**, 52, 13363.

[16] M. A. McGuire, V. O. Garlea, Short-and long-range magnetic order in LaMnAsO. *Phys. Rev. B* **2016**, 93, 054404.

[17] F. Zhang, B. Li, Q. Ren, H. Mao, Y. Xia, B. Hu, Z. Liu, Z. Wang, Y. Shao, Z. Feng, S. Tan, Y. Sun, Z. Ren, Q. Jing, B. Liu, H. Luo, J. Ma, Y. Mei, C. Wang, G. H. Cao, ThMnPnN (Pn = P, As): Synthesis, Structure, and Chemical Pressure Effects. *Inorg. Chem.* **2020**, 59, 2937.

[18] S. Sen, H. Kabbour, H. Ghosh, Pressure-induced antiferromagnetic-tetragonal to nonmagnetic-collapse-tetragonal insulator-metal transition in ThMnAsN. *J. Mater. Sci.* **2023**, 58, 8398.

[19] S. Sen, H. Ghosh, Magnetic-Moment-Induced Metal–Insulator Transition in ThMnXN (X = As, P): A First Principles Study. *Magnetochemistry* **2023**, 9(1), 16.

[20] T. Watanabe, H. Yanagi, T. Kamiya, Y. Kamihara, M. Hirano, H. Hosono, Nickel-Based Oxyphosphide Superconductor with a Layered Crystal Structure, LaNiOP. *Inorg. Chem.* **2007**, 46, 7719.

[21] A. Shibatan, K. Motizuki, T. Nagamiya, Spin Density Wave in Chromium and Its Alloys. *Phys. Rev. B* **1969**, 177, 984.

[22] J. K. Bao, J. Y. Liu, C. W. Ma, Z. H. Meng, Z. T. Tang, Y. L. Sun, H. F. Zhai, H. Jiang, H. Bai, C. M. Feng, Z. A. Xu, G. H. Cao, Superconductivity in Quasi-One-Dimensional $K_2Cr_3As_3$ with Significant Electron Correlations. *Phys. Rev. X* **2015**, 5, 011013.

[23] Z. T. Tang, J. K. Bao, Y. Liu, Y. L. Sun, A. Ablimit, H. F. Zhai, H. Jiang, C. M. Feng, Z. A. Xu, and G. H. Cao, Unconventional superconductivity in quasi-one-dimensional $Rb_2Cr_3As_3$. *Phys. Rev. B* **2015**, 91, 020506.

[24] Z. T. Tang, J. K. Bao, Z. Wang, H. Bai, H. Jiang, Y. Liu, H. F. Zhai, C. M. Feng, Z. A. Xu, and G. H. Cao, Superconductivity with peculiar upper critical fields in quasi-one-dimensional Cr-based pnictides. *Sci. Chin. Mater.* **2015**, 58, 16.

[25] D. J. Singh, A. S. Sefat, M. A. McGuire, B. C. Sales, D. Mandrus, L. H. VanBebber, and V. Keppens, Itinerant antiferromagnetism in $BaCr_2As_2$: Experimental characterization and electronic structure calculations. *Phys. Rev. B* **2009**, 79, 094429.

[26] M. Rotter, M. Tegel, and D. Johrendt, Superconductivity at 38 K in the Iron Arsenide $(Ba_{1-x}K_x)Fe_2As_2$. *Phys. Rev. Lett.* **2008**, 101, 107006.

[27] H. Ghosh and S. Sen, Iron-based superconductors: A brief overview. ISBN: 978-3-659-38098-3, LAP LAMBERT Academic Publishing, Germany, pp. 264 (40 printed pages) (2012).

[28] G. R. Stewart, Superconductivity in iron compounds. *Rev. Mod. Phys.* **2011**, 83, 1589.

[29] U. B. Paramanik, R. Prasad, C. Geibel, and Z. Hossain, Itinerant and local-moment magnetism in $EuCr_2As_2$ single crystals. *Phys. Rev. B* **2014**, 89, 144423.

[30] M.-H. Whangbo, E. Canadell, P. Foury and J. -P. Pouget, Hidden Fermi Surface nesting and charge density wave instability in low-dimensional metals. *Science* **1991**, 252, (5002) 96.

[31] Yining Hu, Tianzhen Zhang, Dongming Zhao, Chen Chen, Shuyue Ding, Wentao Yang, Xu Wang, Chihao Li, Haitao Wang, Donglai Feng and Tong Zhang, Real-space observation of incommensurate spin density wave and coexisting charge density wave on Cr (001) surface. *Nat. Commun.* **2022**, 13, 445.

[32] S. Sen, H. Ghosh, Fermiology of 122 family of Fe-based superconductors: An ab initio study. *Phys. Lett. A* **2015**, 379, 843.

[33] S. Sen, H. Ghosh, Stoner factors of doped 122 Fe-based superconductors: First principles results. *Comput. Mater. Sci.* **2017**, 132, 46.

[34] K. Terashima, Y. Sekiba, J. H. Bowen, K. Nakayama, T. Kawahara, T. Sato, P. Richard, Y.-M. Xu, L. J. Li, G. H. Cao, Z.-A. Xu, H. Ding, T. Takahashi, Fermi surface nesting induced strong pairing in iron-based superconductors. *Proc. Natl. Acad. Sci. U. S. A.* **2009**, 106(18), 7330.

[35] S. Sen, H. Ghosh, Intra-inter band pairing, order parameter symmetry in Fe-based superconductors: A model study. *J. Alloys Compd.* **2015**, 618, 102.

[36] M. Sunagawa, T. Ishiga, K. Tsubota, T. Jabuchi, J. Sonoyama, K. Iba, K. Kudo, M. Nohara, K. Ono, H. Kumigashira, T. Matsushita, M. Arita, K. Shimada, H. Namatame, M. Taniguchi, T. Wakita, Y. Muraoka, T. Yokoya, Characteristic two-dimensional Fermi surface topology of high-T_c iron-based superconductors. *Sci. Rep.* **2015**, 4, 4381.

[37] Zhi-Cheng Wang, Ye-Ting Shao, Yi-Qiang Lin, Shi-Jie Song, Bai-Zhuo Li, Er-Jian Cheng, Shi-Yan Li, Qin-Qing Zhu, Zhi Ren, and Guang-Han Cao (2023). Absence of superconductivity in electron-doped chromium pnictides $ThCrAsN_{1-x}O_x$. *Phys. Rev. B* **108**, 064503.

[38] A. R. Oganov, C. W. Glass, Crystal structure prediction using ab initio evolutionary techniques: principles and applications. *J. Chem. Phys.* **2006**, 124, 244704.

[39] A. R. Oganov, A. O. Lyakhov, M. Valle, How evolutionary crystal structure prediction works - and why. *Acc. Chem. Res.* **2011**, 44, 227-237.

[40] A. O. Lyakhov, A. R. Oganov, H. T. Stokes, Q. Zhu, New developments in evolutionary structure prediction algorithm USPEX. *Comp. Phys. Comm.* **2013**, 184, 1172-1182.

[41] G. Kresse, J. Hafner, Ab initio molecular dynamics for liquid metals. *Phys Rev B* **1993**, 47, 558-561(R).

[42] P. E. Blöch, Projector augmented-wave method. *Phys Rev B* **1994**, 50, 17953-17979.

[43] G. Kresse, J. Furthmüller, Efficiency of ab-initio total energy calculations for metals and semiconductors using a plane-wave basis set. *Comput Mater Sci* **1996**, 6, 15-50.

[44] J. P. Perdew, K. Burke, M. Ernzerhof, Generalized Gradient Approximation Made Simple. *Phys Rev Lett* **1996**, 77, 3865-3868.

[45] S. L. Dudarev, G. A. Botton, S. Y. Savrasov, C. J. Humphreys, A. P. Sutton, Electron-energy-loss spectra and the structural stability of nickel oxide: An LSDA+U study. *Phys. Rev. B* **1998**, 57, 1505.

[46] Y. L. Page, P. Saxe, Symmetry-general least-squares extraction of elastic data for strained materials from ab initio calculations of stress. *Phys Rev B* **2002**, 65, 104104-104117.

[47] M. Kawamura, FermiSurfer: Fermi-surface viewer providing multiple representation schemes. *Comp Phys Commun* **2019**, 239, 197-203.
[48] K. Momma, F. Izumi, VESTA: a three-dimensional visualization system for electronic and structural analysis. *J Appl Cryst* **2008**, 41, 653-658.
[49] S. Maintz, V. L. Deringer, A. L. Tchougréeff, R. Dronskowski, LOBSTER: A tool to extract chemical bonding from plane-wave based DFT. *J Comput Chem* **2016**, 37(11), 1030-1035.
[50] V. L. Deringer, A. L. Tchougréeff, R. Dronskowski, Crystal Orbital Hamilton Population (COHP) Analysis As Projected from Plane-Wave Basis Sets. *J Phys Chem A* **2011**, 115(21), 5461–5466.
[51] R. Dronskowski, P. E. Bloechl, Crystal orbital Hamilton populations (COHP): energy-resolved visualization of chemical bonding in solids based on density-functional calculations. *J Phys Chem* **1993**, 97(33), 8617–8624.
[52] A. Togo, I. Tanaka, First principles phonon calculations in materials science. *Scr Mater* **2015**, 108, 1-5.
[53] R. Hill, The Elastic Behaviour of a Crystalline Aggregate. *Proc. Soc. London A* **1952**, 65, 349.
[54] H. Kabbour, L. Cario, F. Bouchera, Rational design of new inorganic compounds with the ZrSiCuAs structure type using 2D building blocks. *J. Mater. Chem.* **2005**, 15, 3525.
[55] T. Park, M. Ye, L. Balents, Electronic instabilities of kagome metals: Saddle points and Landau theory. *Phys. Rev. B* **2021**, 104, 035142.